PAPER

Check for updates

Concentration-dependent photophysics of InP/ZnS quantum dots: surface still matters despite thick shells

Michael Greben, [ID] *[a] Dmytro Vorontsov, [ID] [a] Petro Khoroshyy, [ID] [b,c]
Michal Gulka [ID] [b] and Jan Valenta [ID] [a]

Core–shell InP/ZnS quantum dots (QDs) are promising non-toxic alternatives to cadmium-based emitters, yet their photophysical stability remains underexplored. Here, we investigate the optical properties of oleic acid-capped InP/ZnS QDs with varying emission energies spanning the visible spectrum. Using steady-state absorption, absolute photoluminescence (PL) quantum yield (QY) measurements, and time-resolved PL spectroscopy, we assess the impact of particle size, concentration, and host environment on radiative performance. Despite thick ZnS shells (6–13 monolayers) that should, in principle, insulate the exciton from the environment, both PL lifetimes and QY exhibit strong, monotonic decreases upon sample dilution. Spectrally resolved lifetime measurements reveal quantum-confinement (QC)-driven trends: larger dots display longer lifetimes, consistent with QC model. However, the dilution-induced suppression of PL efficiency points to surface-related quenching mechanisms where partial desorption of oleate ligands from ZnS surfaces can create defect-mediated nonradiative channels, amplified under ambient oxygen. When plotted against integrated surface area, PL lifetime and QY collapse onto a universal trend across different QD sizes, reinforcing the surface-origin of the observed behavior. Incorporation of QDs into solid polymer matrices further highlights environmental sensitivity: poly(methyl methacrylate) (PMMA) preserves most of the colloidal PL efficiency, whereas polydimethylsiloxane (PDMS) causes severe quenching due to ligand incompatibility and increased oxidative trapping. These results reveal that even in type-I heterostructures with thick shells, excitonic wavefunctions remain susceptible to surface chemistry. The findings underscore the need for ligand engineering and optimized host matrices to achieve stable, high-efficiency InP/ZnS QD emitters for optoelectronic applications.

1. Introduction

Semiconductor quantum dots (QDs) are nanoscale materials widely recognized for their exceptional optical properties, including size-tunable bandgaps, narrow emission profiles, high photoluminescence (PL) quantum yields (QYs) and excellent photostability. These features enable applications in photodetectors, solar cells, bioimaging, light-emitting diodes (LEDs), lasers, color-conversion lighting, and backlit displays.[1–3]

Historically, cadmium (Cd)-based QDs, such as CdSe, dominated the field. In the 2010s, lead (Pb) halide perovskite QDs emerged, offering a combination of outstanding optical performance and facile synthesis, which rapidly accelerated research in this direction.[4] However, the intrinsic toxicity of heavy metals such as cadmium and lead raises significant environmental and health concerns, limiting their use in biomedical and industrial applications, particularly in commercial products and displays. To meet regulatory restrictions on toxic heavy metals, indium phosphide (InP) has emerged as the leading Cd/Pb-free alternative, owing to its low toxicity and biocompatibility.[5] In addition, InP possesses a smaller band gap (~1.35 eV) and a larger exciton Bohr diameter (~10 nm) compared to CdSe (1.74 eV, 5.4 nm), which allows for broad spectral tunability.[6]

Although InP QDs have been investigated since the 1990s, progress was initially hindered by several persistent challenges.[1] Bare InP QDs typically exhibit very low PL QYs (often < 1%) due to their highly reactive surfaces, which readily form

aDepartment of Chemical Physics and Optics, Faculty of Mathematics and Physics, Charles University, Ke Karlovu 3, 121 16 Prague 2, Czechia.
E-mail: leibnits@gmail.com
bInstitute of Organic Chemistry and Biochemistry of the CAS, Flemingovo nam. 2, 166 10 Prague 6, Czechia
cGroup of Advanced Optical Microscopy, Inst. of Biology and Medical Genetics 1st Faculty of Medicine, Charles University, Albertov 2048/4, 128 00 Prague 2, Czechia

defects and oxides.[7] Furthermore, the highly covalent In–P bond complicates nucleation and growth, making it difficult to achieve narrow size distributions. As a result, InP QDs generally display broader ensemble emission compared to their Cd-based counterparts.[3] To overcome these limitations, surface passivation strategies have been extensively pursued, most notably the growth of a wider bandgap semiconductor shell around the InP core. Such core–shell heterostructures effectively passivate surface defects (*e.g.*, dangling bonds), enhance exciton confinement, and substantially increase PL QY. Advances in shell engineering have enabled InP QDs to achieve near-unity PL QYs (approaching 100%), particularly in the green and red spectral regions, with narrow full widths at half maximum (FWHM) of ~35 nm, approaching the performance of state-of-the-art CdSe QDs.[1,8]

Despite these advances, the fundamental understanding of the optical properties and underlying mechanisms governing InP-based core–shell QDs remains less developed than for Cd- or Pb-containing systems.[9] Shell thickness plays a central role in determining optical performance. Thin shells provide incomplete passivation, insufficient exciton confinement, and vulnerability to electron leakage, defect-mediated recombination, and photo-instability, all of which reduce PL QY and broaden emission. In contrast, thicker shells improve core stability by protecting against photo-oxidation and suppressing non-radiative channels such as Förster resonant energy transfer (FRET) and Auger recombination in closely packed ensembles. Robust passivation through a type-I band alignment confines the electron–hole pair within the core, yielding higher PL QY and reduced photobleaching and blinking. However, excessively thick shells can accumulate strain due to lattice mismatch, generating defects that ultimately degrade optical performance. To mitigate such strain, buffer layers with intermediate lattice constants (*e.g.*, ZnSe, ZnSeS, GaP) are often introduced, allowing the growth of much thicker outer shells than is typically achievable with ZnS alone.[10] This balance highlights the existence of an optimal shell thickness that provides effective passivation and stability while avoiding strain-induced defects – a design principle that guides much of current research.

Beyond this established framework, however, remains a critical unresolved question: can InP cores with nominally "thick" ZnS shells truly be considered completely isolated from their environment, such that their optical properties become insensitive to surface states? Current evidence suggests that this is not the case. Nevertheless, systematic studies explicitly addressing the role of the ZnS surface in thick-shell InP systems are still limited. To bridge this gap, we investigate three ensembles of oleic acid (OA)–capped InP/ZnS QDs, emitting in the green, orange, and red spectral regions, each with different shell thicknesses. By varying concentration and surrounding medium, we show that surface-related effects continue to play a decisive role in determining the optical properties, even in QDs with ostensibly "thick" ZnS shells.

2. Materials and methods

The OA-capped core–shell InP/ZnS QDs of three mean sizes (Table 1) were purchased from Sigma-Aldrich with a nominal mass concentration of 5 mg ml^{-1} in each stock solution.

The QD ensembles emit in green (QD-G), orange (QD-O) and red (QD-R) spectral regions (Fig. 1).

Aliquots of fresh stock solutions were diluted in toluene to obtain a series of QD suspensions with relative concentrations
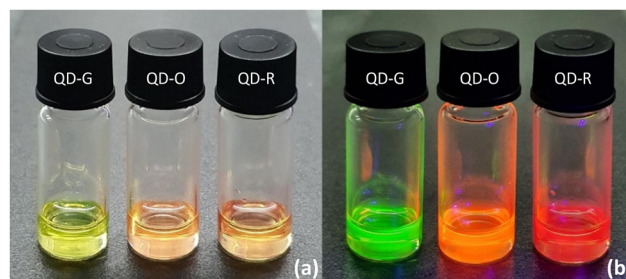

Fig. 1 Suspensions of OA-capped core–shell InP/ZnS QDs in toluene, emitting in the green (QD-G), orange (QD-O), and red (QD-R) spectral regions (from left to right), shown under (a) ambient and (b) UV illumination.

Table 1 Summary of the optical and structural properties of green- (QD-G), orange- (QD-O), and red-emitting (QD-R) oleic-acid capped InP/ZnS core/shell QDs. Parameters include the absorption and PL peak positions, Stokes shift, valley depth (VD) in absorbance, PL FWHM, and PL QY (for stock solution), as well as mean core/shell sizes determined by TEM and optical methods. The mean shell thickness is expressed both in nanometers and in terms of the number of ZnS monolayers (MLs), assuming a nominal monolayer thickness of ~0.27 nm

Characteristics	QD-G	QD-O	QD-R
Abs. peak	507 nm	563 nm	618 nm
PL peak	537 nm	607 nm	644 nm
Stokes shift	30 nm	44 nm	26 nm
VD	0.38	0.05	0.2
PL FWHM	39 nm	50 nm	44 nm
PL QY (stock sol.)	25%	38%	45%
Mean diameter (core + shell, TEM)	6.0 ± 0.5 nm	7.5 ± 0.5 nm	9.5 ± 0.5 nm
Mean diameter (core only, optical)	2.2 ± 0.2 nm	2.8 ± 0.2 nm	3.5 ± 0.3 nm
Mean shell thickness (in QD radius)	1.9 ± 0.4 nm	2.4 ± 0.4 nm	3 ± 0.4 nm
No. of mean shell MLs	5.7–8.3	7.4–10.0	9.6–12.6

in the range 100%–6.25%. The samples were sealed either in larger 0.5 × 0.5 cm² cuvettes (sample volume of 0.4 mL, 50%–6.25% rel. mass concentrations) or smaller 0.1 × 1 cm² cuvettes (sample volume 0.3 mL, 100%–75% rel. mass concentrations).

For the incorporation of QDs into poly(methyl methacrylate) (PMMA), InP/ZnS QD solutions with relative mass concentrations of 12.5% and 50% were mixed with a ∼35.3 wt% PMMA solution, prepared by dissolving a UV-grade PMMA cuvette (Kartell) in toluene. The mixtures were left to evaporate in the dark. To ensure that the resulting composites retained the same QD mass concentrations (12.5% and 50%) as the initial solutions, the mass of PMMA was adjusted to match the mass of toluene.

For the incorporation of QDs into polydimethylsiloxane (PDMS), InP/ZnS QD solutions with relative mass concentrations ranging from 6.25% to 50% were mixed with freshly prepared PDMS (Sylgard 184 kit), obtained by combining the base and curing agent in a 10 : 1 mass ratio. The mixtures were then allowed to cross-link at room temperature under reduced pressure to facilitate toluene evaporation. As with the PMMA composites, the mass of PDMS was adjusted to match the mass of toluene, ensuring that the resulting composites had approximately the same QD mass concentrations as the initial solutions.

The absorption spectra were taken using a double-beam spectrophotometer (Specord 250, Analytik Jena) with the pure solvent as a reference sample.

Time-resolved (TR) PL decay kinetics were acquired using a commercial Leica TCS SP8 microscope. Excitation was provided by a 405 nm diode laser delivering 100 ps pulses at a repetition rate of 1 MHz. The excitation power was approximately 1 μW, and an air objective (10×, NA = 0.3) was used. The PL signal was collected using three Leica SP8 HYD detectors across three spectral windows (510–580 nm, 586–620 nm, and 620–800 nm), with the signals either summed after collection or analyzed separately. Instrument response function (IRF) was in sub-ns scale which was significantly faster than PL decay kinetics and therefore, its deconvolution was deemed unnecessary. Collected TR PL data were processed using home-written Python code where intensity-averaged recombination lifetimes were calculated employing fitting-free (integration) model:

$$\bar{\tau}_{\text{int}} = \frac{\int_0^\infty t I(t)\,\mathrm{d}t}{\int_0^\infty I(t)\,\mathrm{d}t} \qquad (1)$$

where t stands for the time since the beginning of decay and $I(t)$ represents PL intensity signal as a function of time.

For more details including lifetime uncertainty estimates, see ref. 11 and 12.

Absolute PL QY measurements were performed using a tunable excitation source based on a laser-driven light source (LDLS, Energetiq) coupled to a 15 cm monochromator (Acton SP-2150i). This configuration provided a weak irradiance at the specimen, approximately 10 μW cm⁻². Unless otherwise specified, the default excitation wavelength was 405 nm. Sample emission was analyzed with a 30 cm imaging spectrograph (Acton SP-2300i) equipped with a liquid-nitrogen-cooled, back-illuminated CCD detector (Spec-10:400B, Princeton Instruments). All measurements were conducted with the specimen housed inside a 10 cm-diameter integrating sphere (Sphere Optics), with fused-silica fiber bundles used to deliver the excitation beam and collect the fluorescence. The entire optical system was radiometrically calibrated against a secondary standard of spectral irradiance, a 45 W tungsten–halogen lamp (Newport Oriel). The PL QY values obtained under these conditions carry an uncertainty of 1–4%, determined primarily by fluctuations in the excitation source. Additional experimental specifics are provided in ref. 13. The PL spectra presented in this study were acquired concurrently with the PL QY measurements.

To determine the particle sizes, transmission electron microscopy (TEM) was performed. A 1 μL aliquot of the sample suspension was deposited onto TEM grids coated with a 5 nm carbon film, immediately blotted with filter paper, and allowed to dry for at least 10 minutes. TEM images were acquired using a JEOL JEM-F200 microscope (Japan) operated at 200 kV and equipped with a Gatan Alpine Vista direct electron detector (USA) at nominal magnifications ranging from 50k to 100k. The particle size distributions were extracted from the TEM micrographs using the *Fiji* (ImageJ) software package.[14]

3. Results and discussion

3.1. Absorption and PL spectra

Fig. 2 summarizes the normalized PL and absorption spectra of the three samples across multiple dilutions. The maxima of the first excitonic absorption (emission) bands are near 507 (537) nm, 563 (607) nm, and 618 (644) nm, respectively, evaluated over the mid-range of relative mass concentrations (25–75%).

In absolute terms, the peak absorbance A_{10} exhibits a linear dependence on the relative particle concentration (Fig. S1), consistent with the Beer–Lambert law:[15]

$$A_{10} = \alpha_{10} l = \varepsilon_{10} c_{\text{V}}^{\text{QD}} L = \varepsilon_{10} \frac{[c_{\text{m}}^{\text{tot}} - c_{\text{m}}^{\text{lig,t}}]}{\rho_{\text{QD}}\left(\frac{4}{3}\pi R^3\right) N_{\text{A}}} L \qquad (2)$$

where α_{10} is the decadic absorption coefficient, c_{V}^{QD}, $c_{\text{m}}^{\text{tot}}$ and $c_{\text{m}}^{\text{lig,t}}$ are the particles volume molar concentration, mass concentrations of the solids content and organic ligands, respectively, ρ_{QD} stands for the effective particle density, ε_{10} is the decadic molar extinction coefficient, L is the optical path length; and R is the particle radius.

The R^{-3} scaling of the absorbance arising from particle volume in eqn (2) is consistent with the theoretical prediction that the absorption coefficient of QDs scales inversely with R^3. This arises because the coefficient is normalized to particle volume, yielding $\alpha = (a_{\text{B}}/R)^3$, where a_{B} is the exciton Bohr radius.[16] In contrast, the mass of the bound ligand layer scales
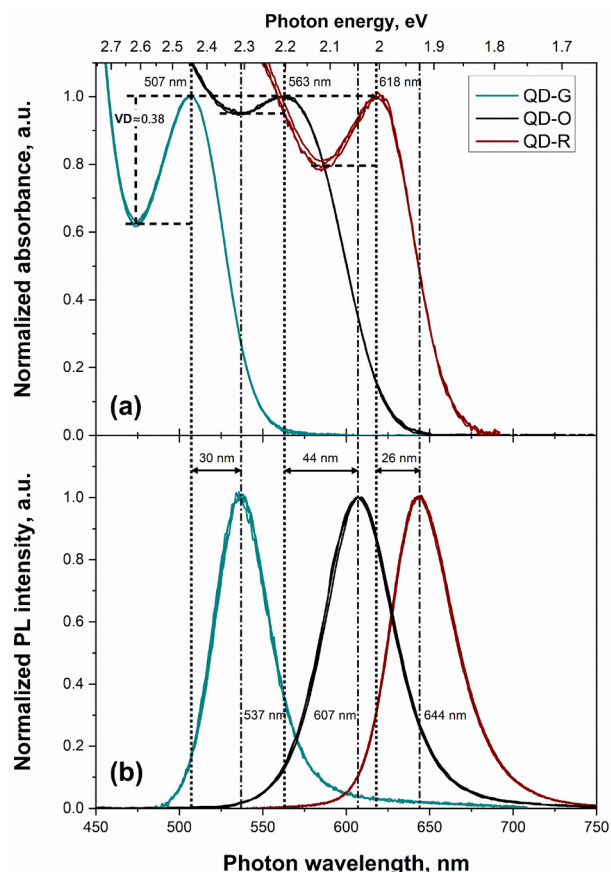
Fig. 2 Normalized absorption (a) and PL (b) spectra of QD-G (dark cyan), QD-O (black) and QD-R (wine) ensembles. PL spectra are collected under 405 nm weak light excitation. The dotted and dashed-dotted vertical lines indicate the absorption and emission peak positions, respectively. The horizontal dashed lines serve as eye-guides for the peak and valley absorbance. Vertical dashed line represents the valley depth for QD-G sample.

as R^2, *i.e.*, with particle surface area. As shown in eqn (S7) (SI), the total (bound + free) ligand mass fraction in the total solids scales approximately as $(kR + 1)^{-1}$, where k is effectively constant for a given ligand and coverage. This dependence is evidently much weaker than the $c_V^{QD} \sim R^{-3}$ scaling in eqn (2). Consequently, at fixed solids mass concentration c_m^{tot}, the absorbance in Fig. S1 decreases with increasing mean QD size primarily because the number concentration of particles falls (see eqn (S8)). The fraction and absolute mass of bound oleate likewise decrease with increasing particle size (eqn (S6) and (S7)).

Eqn (2) can be used to convert c_m^{tot} into the particle molar concentration c_V^{QD} (see SI and eqn (S11) for details). In these calculations, the free-ligand concentration in solution was assumed to scale linearly with the bound-ligand content. This assumption reflects the well-established equilibrium between surface-bound and unbound oleate species in colloidal nanocrystal dispersions, as confirmed by numerous NMR (^{1}H, DOSY, NOESY) studies on OA-capped QDs.[17,18] The coexistence of bound and free or weakly associated ligands is a common feature of colloidal QD surface chemistry[19,20] and has been

observed even after extensive purification.[21] Tables S1 and S2 summarize the resulting estimates for two scenarios: 0% and 50% free ligand (relative to the bound-ligand mass). In both cases, QD-G contains about 1.8× more particles than QD-O, and QD-O contains about 1.9× more particles than QD-R. Although the absolute molar concentrations are approximate (we adopt literature oleate coverages), the ratios of sample concentrations are robust, with an estimated uncertainty of ~5% (SI, Tables S3 and S4). These relative molar concentrations are used in subsequent analyses.

An idealized description[15] predicts atom-like discrete transitions in both absorption and emission for QDs with three-dimensional spatial confinement. In real ensembles, homogeneous and inhomogeneous broadening and possible light-scattering backgrounds smear discrete features into a structured continuum. Because the ensemble linewidth reflects the convolution of band-gap distributions, it is sensitive to the particle size distribution (PSD). The present ensembles differ in PSD, as evidenced by two observations. First, both the excitonic absorption peak (Fig. S2) and the PL peak (Table 1) broaden from QD-G to QD-R and QD-O. Second, we evaluate the valley depth (VD), an indirect dispersity metric:

$$VD = \frac{A_{peak} - A_{valley}}{A_{peak}} \tag{3}$$

where A_{peak} and A_{valley} are the peak and valley absorbances, respectively (see Fig. 2).

Size-sorting studies show that improved monodispersity increases the peak/valley ratio.[10] Here, VD follows the same trend (Table 1): QD-G exhibits the largest VD ≈ 0.38, indicative of a relatively narrow PSD.[22] Note that ZnS-coated QDs are, *a priori*, expected to exhibit broader PSDs than bare InP samples.[23,24]

For a direct comparison of band-edge absorption and emission, we focus on the QD-G ensemble (Fig. 3). To resolve the excitonic band-edge peak, we subtract a baseline near the band edge, treating the spectrum outside and near E_g as a featureless background approximated by an exponential function.[25,26] The resulting near-Gaussian absorption peak closely overlaps the normalized PL band after compensating the Stokes shift, supporting the interpretation that both arise from the same fundamental electronic transitions.

Fig. 3 (blue circles) shows the external PL QY *versus* excitation wavelength. Organic fluorophores generally obey Kasha's and Vavilov's rules,[27] implying excitation-independent emission spectra and QY in condensed media, respectively. QDs typically obey Kasha's rule but not Vavilov's rule.[28] The intrinsic PL QY of the dots, governed by the radiative-to-nonradiative competition after hot-carrier cooling can be observed at sufficiently high-energy excitation at 400 nm < λ_{exc} ≤ 440 nm. Because hot carriers relax to the band edge on femtosecond timescales,[28] the QY becomes nearly independent of the excess photon energy. At still higher non-resonant excitation energies (λ_{exc} < 400 nm), PL QY can decrease,[28] as excitation well above the InP band edge can also populate shell and near-interface states. The photogenerated carriers then (i)
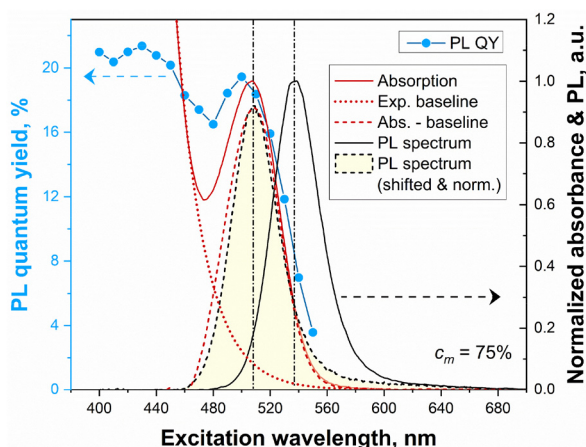
Fig. 3 Normalized absorption (dark red solid line) and PL (black solid line) spectra (right axis) of QD-G sample at relative mass concentration 75%. The absorption baseline at energies above the first excitonic peak is approximated with an exponent (dark red dotted line). The first excitonic peak absorption (dark red dashed line) is resolved after the baseline subtraction. Adjusted PL band (black dashed line, filled yellow area) is spectrally shifted to compensate for the Stokes shift. The blue symbols represent the PL QY as a function of excitation wavelength (left axis) for the same sample. The dashed arrows point to the relevant axes.
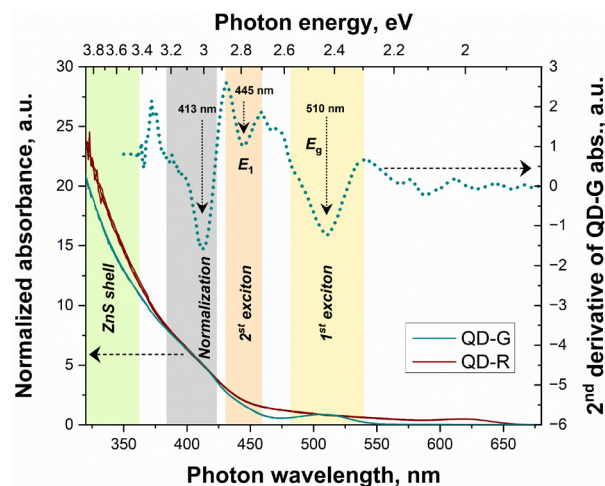

Fig. 4 Normalized absorption spectra (left axis) of QD-G (dark cyan solid line) and QD-R (wine solid line) ensembles. The second derivative (dark cyan dashed line) of the QD-G absorption (right axis) is used to pinpoint electronic transitions. Shaded bands highlight the spectral regions attributed to the first excitonic transition E_g (pale yellow), the second excitonic transition E_1 (beige), the wavelength interval chosen for spectral normalization (grey), the ZnS-shell absorption (light green). Vertical dotted arrows mark the major derivative local minima. The dashed arrows point to the relevant axes.

cool and localize to the core, while (ii) a fraction is captured by interfacial or deep traps, both processes occurring on the picosecond timescale.[29,30] This partially depletes the band-edge population, which subsequently recombines radiatively over tens of nanoseconds (section 3.3). Under resonant excitation at the band-edge absorption peak (no excess energy), PL QY also locally increases: generating electron–hole pairs directly at the band edge avoids hot-phonon relaxation and interfacial capture, yielding a QY close to the intrinsic value. Similar resonant enhancements have been reported for InP[28] and CdSe[31] QDs. The local minimum in PL QY near 480 nm lies between the first and second lowest-energy absorption features and likely reflects a reduced density of states; a similar dip has been observed for CdSe QDs.[31] At sub-gap excitation energies, the QY drops steeply due to absorption–emission spectral overlap and the strong influence of reabsorption: higher-energy photons emitted by smaller dots are reabsorbed by larger dots, increasing the probability of nonradiative recombination. Sub-gap traps may further contribute to the QY decrease.

Fig. 4 shows the absorbance of the QD-G and QD-R ensembles over a broader spectral range extending into the UV, where transitions above the band-edge (E_g) are evident. The spectra are normalized near 400 nm, a region well above the respective bandgaps where confinement effects are expected to be less pronounced.[32] In this region, the density of states approaches the continuum, and the extinction coefficient ε_{10} should approach bulk-like values. However, studies on PbS QDs[33] and CdSe QDs[34] have demonstrated that, even at excitation wavelengths far above the bandgap (300–400 nm), QC features can still be observed.

To resolve hindered features in the absorption spectrum A of the selected QD-G sample, we calculated its second derivative ($d^2A/d\lambda^2$), shown in Fig. 4 (right axis). Two negative extrema are observed near 510 nm (2.43 eV) and 445 nm (2.79 eV), which we attribute to the first and second (the next-higher energy direct interband transition) excitonic transitions, respectively. Between these two peaks lies a spectral region of reduced electronic density of states, as also discussed in Fig. 3. Density functional theory (DFT) calculations for QDs of similar size (D = 2.3 nm) predicted $E_g \approx 2.52$ eV and $E_1 \approx 2.85$ eV.[35] By aligning the DFT calculations to the first excitonic peak of our QD-G sample, we obtain an estimated energy of the second excitonic transition near 2.76 eV, which agrees well with the experimental value in Fig. 4. The agreement is particularly reasonable given that the DFT calculations were performed for core-only InP QDs. The increase in absorbance below 350–370 nm (compare QD-G and QD-R in Fig. 4) arises[6,36] mainly from transitions in the ZnS shell material, with additional contributions from light scattering. This assignment is consistent with the bandgap of bulk zinc blende ZnS, which lies at 3.61 eV (343 nm).[37] A distinct hump near 413 nm is clearly observable, and its spectral position remains fixed irrespective of the QD mean size. This feature can be assigned to an artifact of the second-derivative method, where curvature effects can mimic absorption features.

3.2. Size of the particle core and shell

Fig. S3–S5 show TEM micrographs acquired at different magnifications together with the corresponding size histograms. Particles with small sizes ≤2 nm, which approach the limit of

experimental resolution, were excluded from the analysis. The QDs exhibit a variety of irregular shapes, while their size distributions are symmetric and approximately Gaussian. The extracted mean QD sizes (core + shell) are in good agreement with the values reported by the vendor (Sigma-Aldrich) and are summarized in Table 1.

To estimate the shell thickness, the size of the InP cores must first be known. This is typically obtained from a sizing curve,[25] which empirically relates the mean size of isotropically shaped QDs to corresponding changes in their optical response and is specific to each material. Since the PL peak incorporates both a sample-specific Stokes shift and potential self-absorption effects, band-edge absorption energies are usually employed for constructing sizing curves.

A non-trivial issue arises when defining the physically and optically relevant "true" size of QDs in core–shell systems. In general, InP/ZnS QDs are known to exhibit type-I band alignment,[38,39] in which charge carriers are primarily confined within the InP core. However, the assumption of infinitely strong confinement by the ZnS shell is likely unrealistic, given the similar electron affinities of InP (4.4 eV) and ZnS (3.9 eV). This small conduction band offset may not provide sufficient confinement for electrons,[40] allowing partial delocalization of their wavefunction into the shell. A more realistic picture is that the ZnS shell provides a finite potential barrier rather than an abrupt vacuum interface, permitting partial leakage of the electron wavefunction into the shell. Experimentally, this effect is often manifested as a minor redshift[32,38,41,42] of the band-edge absorption following ZnS coating of InP cores. In such cases, optically determined core sizes may be slightly overestimated and are thus better regarded as upper limits.

A comparison of InP (bandgap 1.35 eV) and CdSe (bandgap 1.74 eV) highlights the unique sensitivity of InP QDs to quantum confinement. The exciton Bohr radius of InP (~10 nm) is nearly twice that of CdSe (~5.4 nm), implying that for QDs smaller than 5 nm, InP experiences significantly stronger confinement effects.[6] Consequently, InP QDs are more optically responsive to small changes in size. For example, to span the same absorption spectral range, the required variation in InP volume is only about half that of CdSe.[43] This heightened sensitivity, coupled with the influence of a ZnS shell of varying thickness, likely accounts for the diversity of reported sizing curves (Fig. S6), which exhibit distinct spectral dependences. In this work, we adopted sizing curves reported by Lee et al.[44] and Cho et al.[45] as the lower and upper bounds, respectively, for estimating QD sizes. The resulting InP core sizes, ZnS shell thicknesses, and the corresponding number of ZnS monolayers (MLs) are summarized in Table 1. The latter were calculated assuming an average monolayer thickness of 0.27 nm for cubic ZnS.[22,38]

Thin single outer shell layer of ZnS has been shown to be insufficient to passivate InP cores and protect them from surface traps.[46] In contrast, ZnS shells a few monolayers thick (2–5 MLs) have been found in various studies[6,47] to maximize the PL QY and minimize the FWHM of the PL band. However, excessively thick shells may introduce significant lattice strain

at the core–shell interface, generating defects that ultimately reduce PL QY and broaden the band-edge emission due to strain-induced effects.[22] For example, a PL QY of approximately 70% was reported for InP/ZnS QDs with a 3 ML ZnS shell, whereas it decreased to about 20–30% when the shell thickness reached 5–6 MLs.[22,48] This understanding currently represents the state of the art in interpreting the optical properties of core–shell QDs. As shown in Table 1, the QD ensembles investigated here possess relatively thick shells (approximately 6–13 MLs). Such shells are typically considered sufficient to isolate carrier wavefunctions and suppress photophysical perturbations from the external environment, such as ligand interactions and surface defects.[38,49] Nevertheless, as demonstrated in the following sections, varying the QD concentration reveals that even thick ZnS shells consisting of many atomic layers do not render the core–shell heterostructure completely insensitive to its surroundings.

3.3. Spectral dispersion of PL lifetime

It has been demonstrated that ZnS shell coating not only functions as a protective layer but also leads to longer PL decay lifetimes compared to core-only InP QDs. This effect arises directly from the effective isolation of excitons from non-radiative trap channels at the surface.[49–51] For the same reason, increasing the ZnS shell thickness generally leads to longer PL lifetimes relative to thinner shells, up to a certain critical thickness.[51] Beyond this limit (typically 3–10 MLs), the lifetime often decreases, which is usually accompanied by a decline in PL QY due to the accumulation of lattice strain within the heterostructure.[38,52] In general, prolonged PL lifetimes are frequently associated with improved surface passivation and higher optical quality when the emission originates from band-edge states, as they indicate a reduction of non-radiative decay channels under the assumption of a fixed radiative rate. Nevertheless, extended lifetimes can also arise from radiative recombination through shallow trap or defect states. In either case, longer PL lifetimes may be advantageous for fluorescence lifetime imaging applications.[53]

We performed spectrally resolved TR PL measurements under 405 nm excitation to probe size-selected subfractions of the QD-O ensemble at stock concentration. The PL decay transients were strongly non-exponential (Fig. S7), so we employed a fitting-free model (see eqn (1)) to extract intensity-averaged lifetimes (Fig. 5, right axis).[12] The spectral dispersion of PL lifetimes revealed an approximately exponential dependence on the emission wavelength. For the smaller QDs in the ensemble (left shoulder of the emission band), the PL lifetime remained nearly constant, approximately a few tens of nanoseconds, up to the mean ensemble size (Fig. 5, green line). A marginal increase in lifetime at shorter emission wavelengths was at the limit of experimental precision and can be attributed to increasing data uncertainty near the edge of the emission band. A similar invariance of PL lifetime over the 2.1–2.4 eV range was reported by Almeida et al.[54] In contrast, for larger QDs (right shoulder of the PL band), lifetimes increased markedly, reaching approximately 120 ns at 750 nm.
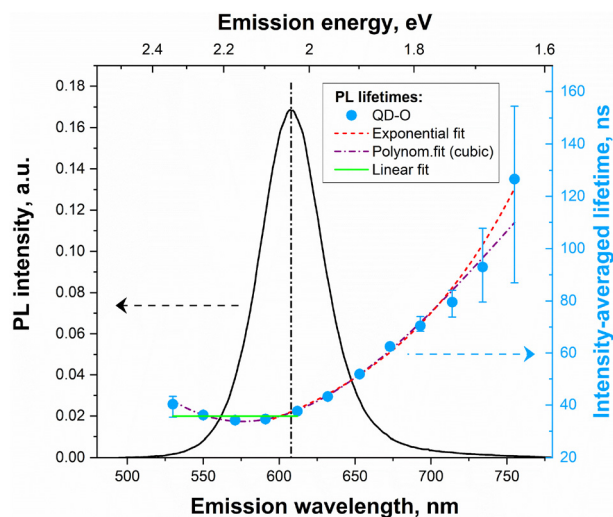
Fig. 5 PL spectrum (black solid line, left axis) of QD-O stock solution without dilution. Spectral dispersion of PL intensity-averaged decay life-times (light blue circles, right axis) of the sample. Various fits serve as an eye-guide. Vertical dashed-dotted line designates the position of PL peak. The dashed arrows point to the relevant axes.

A comparable trend of increasing PL lifetime toward lower emission energies has been reported in earlier studies of InP-based QDs.[54–56] It is also generally recognized that blue- and green-emitting QDs typically exhibit lower performance compared to their red-emitting counterparts.[5,52,57]

From a theoretical perspective, this dependence can be rationalized as follows. The radiative decay rate is proportional to the spontaneous emission probability, which can be expressed using Fermi's golden rule:[11,58]

$$\Gamma_{\mathrm{r}} = \frac{1}{\tau_{\mathrm{r}}} = \frac{F_{\mathrm{P}}}{\tau_{\mathrm{r}}^{\mathrm{vac}}} = \frac{2e^2 F_{\mathrm{P}}}{\hbar^2 m_0 c^3}(E_{\mathrm{g}}^{\mathrm{em}})^2 f(E_{\mathrm{g}}^{\mathrm{em}}) \quad (4)$$

where $\tau_{\mathrm{r}}^{\mathrm{vac}}$ is the radiative lifetime in vacuum, F_{P} denotes the Purcell factor which adjusts for medium corrections, $f(E_{\mathrm{g}}^{\mathrm{em}})$ represents the oscillator strength (OS) of lowest-energy exciton state at $E_{\mathrm{g}}^{\mathrm{em}}$, with $\hbar$ and c signifying the reduced Planck's constant (equals $h/(2\pi)$) and speed of light in vacuum, respectively. e and m_0 indicate the free-electron charge and mass, respectively.

Within the effective mass approximation (EMA), strong QC, in which the electron and hole are independently quantized, occurs when $\chi = R/a_{\mathrm{B}} < (\sim 2–3)$.[59] As indicated in Table 1, this condition is satisfied for all ensembles studied ($\chi < 0.2$), confirming that the QDs in this work are firmly in the strong QC regime. EMA calculations predict that the OS should depend only weakly on size in this regime.[60,61] Accordingly, eqn (4) implies that the radiative lifetime increases (Fig. 5) with emission wavelength $\lambda_{\mathrm{em}} = 2\pi\hbar/E_{\mathrm{g}}^{\mathrm{em}}$ as a direct consequence of QC effect. The spectral dependence of the OS further accentuates this trend. Indeed, for InP QDs the OS has been shown to increase with emission energy,[54,62] similar to observations in IV–VI[58] and II–VI[63] semiconductor

QDs. The underlying reason is that larger QDs act as more effective charge "antennas", despite the reduced overlap of electron and hole wavefunctions compared to smaller dots. When normalized by particle volume, however, the OS exhibits the opposite trend.[54]

DFT calculations have predicted a linear dependence of the exciton radiative decay lifetime on InP dot size,[35] a trend also observed in CdSe and PbS QDs.[58,64] In the present study, we observed a linear dependence of the recombination rate on emission energy within a selected size range. The total decay rate can be expressed as a sum of radiative and non-radiative contributions, with the radiative term described by a momentum form of OS in eqn (4):

$$\Gamma_{\mathrm{PL}} = \frac{1}{\tau_{\mathrm{PL}}} = \frac{1}{\tau_{\mathrm{nr}}} + \frac{F_{\mathrm{P}}}{\tau_{\mathrm{r}}^{\mathrm{vac}}} = \frac{1}{\tau_{\mathrm{nr}}} + \frac{4e^2 F_{\mathrm{P}}}{3\hbar^2 m_0{}^2 c^3}|p_{\mathrm{fi}}|^2 E_{\mathrm{g}}^{\mathrm{em}} \quad (5)$$

where τ_{nr} is the non-radiative lifetime, $|p_{\mathrm{fi}}|^2$ matrix element of the momentum.

Assuming that $|p_{\mathrm{fi}}|^2$ is nearly size-independent within the considered size range, as reported for PbS[58] and CdSe (CdTe)[65] QDs, the total decay rate Γ_{PL} can show an approximately linear dependence on emission energy according to eqn (5). Indeed, excluding the smallest particles, where the decay rate becomes size-independent, our data reveal a linear relation between the decay rate and the energy gap (Fig. S8). The size independence of the decay rate for sufficiently small dots can be explained either by the matrix element term $|p_{\mathrm{fi}}|^2$, which may become[58] size dependent and compensate the term $E_{\mathrm{g}}^{\mathrm{em}}$, or by a diminishing contribution of the non-radiative component $1/\tau_{\mathrm{nr}}$ with decreasing dot size. The latter explanation is unlikely, since the opposite trend is typically expected for smaller QDs due to (i) stronger QC, which lowers the effective confinement barrier of the shell, and (ii) the increasing surface-to-volume ratio, which enhances the likelihood of exciton trapping at non-radiative surface states.

3.4. Dependence of PL lifetime and QY on sample concentration

Surprisingly, we were unable to find any comprehensive study addressing the optical stability of core–shell InP-based QDs as a function of concentration. Toufanian *et al.* predicted, using EMA modelling,[38] that InP/ZnS heterostructures with core diameters larger than 2 nm fall exclusively within the type-I localization regime. Considering the very thick shells of the core–shell heterostructures studied here (see Table 1), we anticipated effective isolation of the confined exciton, presumably located in the InP core, from surface effects. Therefore, no modulation of the optical properties upon dilution was expected.

Experimentally, however, PL lifetimes exhibited a strong exponential dependence on concentration, as shown in Fig. 6a. In contrast to Fig. 5, here the average decay lifetimes were calculated from spectrally integrated PL curves. When comparing smaller (QD-O) and larger (QD-R) QDs, the former exhibited slightly stronger sensitivity to mass concentration, which becomes apparent when the QD-R curve is normalized
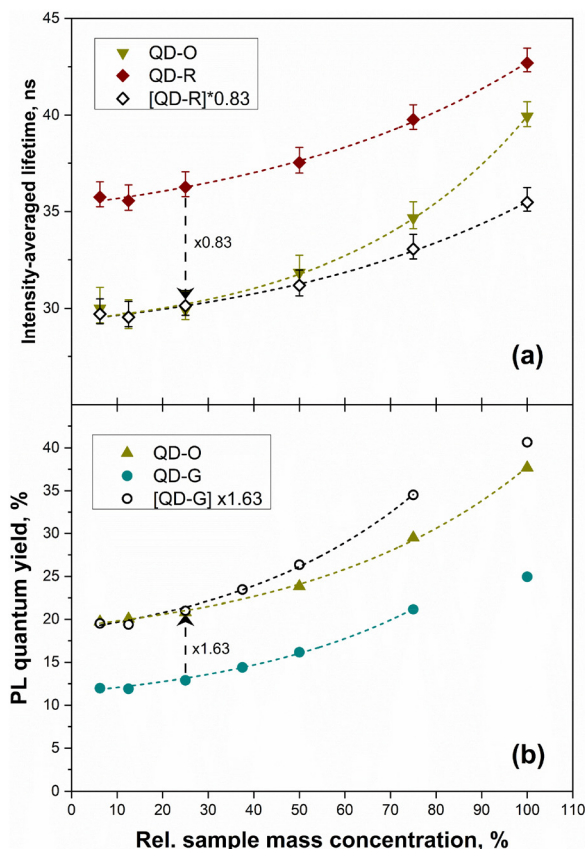
Fig. 6 Concentration-dependent photophysics of QD-G (dark cyan circles), QD-O (dark yellow triangles) and QD-R (wine diamonds) ensembles. (a) Intensity-averaged PL decay lifetime, obtained from spectrally integrated PL time traces. (b) Absolute PL QY, measured with an integrating-sphere setup. In both panels (a) and (b) the excitation was done with 405 nm laser. To facilitate direct comparison with QD-O, the open symbols reproduce the data for QD-R and QD-G after multiplication by the factors indicated in the panels (0.83 and 1.63, respectively). The sample mass concentration expressed as a percentage of the as-prepared stock dispersion (100% = 5 mg mL^{-1}). Dashed curves are guides to the eye. For every batch, both PL decay lifetime and QY decrease monotonically upon dilution, evidencing a universal loss of apparent radiative performance at lower concentrations.

(Fig. 5, black open diamonds). However, recalculating relative mass concentrations into relative molar concentrations of particles (see Tables S1 and S2) reveals an opposite trend (Fig. S9a), which will be discussed further below.

Once concentration effects are considered, it is important to examine potential contributions from resonance energy transfer (ET) and photon reabsorption in highly concentrated samples. In both cases, small QDs can act as energy donors and large QDs as acceptors. Significant ET or reabsorption would be expected to shorten PL lifetimes of smaller dots, while simultaneously lengthening the lifetimes of larger ones within the ensemble.[66] To test this, we monitored variations in PL lifetimes across different spectral regions as a function of concentration (Fig. S10). All three lifetime functions changed synchronously with concentration, ruling out ET and reabsorption as the origin of the observed concentration dependence.

This outcome is consistent with expectations in the case of ET, since thick ZnS shells should suppress photophysical interactions between small and large InP cores within the same ensemble.[67]

However, we were still able to capture the elusive reabsorption of photons from smaller QDs (larger band gaps) by larger ones (smaller band gaps), an effect that is expected to manifest as a PL redshift in highly concentrated samples. Furthermore, because light from smaller QDs is underrepresented in spectra affected by reabsorption, a slight narrowing of the PL band is also expected when comparing dense and diluted samples. Indeed, we observed a subtle PL redshift of several nanometers (Fig. S11) together with a marginal decrease in PL band FWHM (Fig. S12) across all color ensembles as the relative mass concentration varied from 6.25% to 100%. These effects confirm the presence of slight photon reabsorption, though it was too weak to induce measurable changes in decay lifetimes (Fig. S10).

One possible explanation for the lifetime–concentration dependence in Fig. 6a could be variations in the radiative rate triggered by changes in the solvent refractive index.[68] Within this assumption, the effective dielectric permittivity of the medium would be expected to increase with concentration, since the permittivity of the semiconductor core–shell materials is much higher[11,68] than that of toluene. This increase should enhance the Purcell factor and thereby shorten the radiative lifetime with increasing concentration (see eqn (4)). Contrary to this expectation, we observed the opposite trend (Fig. 6a), suggesting that solvent refractive index effects are negligible in our case.

To disentangle radiative and non-radiative contributions, we evaluated the concentration dependence of PL QY (Fig. 6b). Using QD-G and QD-O ensembles as examples, we show that the PL QY decreases with dilution, with a similar trend observed across different color ensembles. As with lifetimes, smaller QDs (QD-G) displayed a steeper PL QY dependence on mass concentration than larger ones (QD-O). However, when expressed in terms of relative molar concentration (Fig. S9b), the trend reverses. Fig. S13 reveals a strong linear correlation between PL QY and decay lifetime, as evidenced by the fitted regression line. This implies that for relative assessment of emission efficiency, the analysis of PL decay traces alone is often sufficient. Such behaviour is ubiquitous among quantum-dot systems and has also been reported, for example, in PbS QDs.[69]

Finally, if the fraction of dark QDs (*i.e.*, QDs that absorb but do not emit light) in the ensemble is assumed to be negligible, then the PL QY (η_{QY}) should equal the internal quantum efficiency (η_{IQE}):

$$\eta_{QY} \approx \eta_{IQE} = \frac{\Gamma_{rad}}{\Gamma_{PL}} \quad (6)$$

Eqn (6) can be used to separate radiative and non-radiative contributions to emission, as shown in eqn (S12) and Fig. S14. The radiative rate decreases by a factor of 1.4 when the relative concentration is reduced from 100% to 12.5%. Over the same concentration range, the non-radiative rate increases by a factor of 1.7. These results indicate that dilution induces

changes in the ensemble that deteriorate radiative recombination while substantially enhancing the non-radiative contribution.

Next, we briefly discuss the possible physical origin of this phenomenon. The observations (Fig. 6 and S9) for OA-capped core–shell structures resemble the behaviour previously reported for OA-capped core-only semiconductor QDs.[11,70,71] In the latter case, this effect is often attributed to concentration-selective ligand desorption dynamics, which introduce surface defects upon dilution. Indeed, as the dispersion is diluted, the chemical potential of bound ligands decreases, meaning that some surface-bound oleates may desorb into solution. In our case, oleate is a long-chain ligand that binds to Zn^{2+} on the ZnS shell.[72] If a fraction of these oleates detach during dilution, two consequences are possible: (i) creation of patchy regions on the shell with incomplete organic passivation, and (ii) increased accessibility of these exposed sites to reactive agents in solution. Notably, the ZnS surface without full oleate coverage contains unsaturated Zn or S sites that act as traps. Such undercoordinated surface atoms serve as non-radiative recombination centres that quench PL. Moreover, since all measurements were performed under ambient conditions, dissolved oxygen in toluene could interact with QDs. Upon ligand desorption, oxidation of the surface may occur, with adsorbed O_2 acting as a trap for charge carriers. For future studies, replacing the native oleate ligands with more strongly binding species such as alkylthiols would be a promising strategy to probe the impact of ligand binding strength on the observed concentration-dependent PL trends.

There is, however, a notable difference between core-only and core–shell QDs. Core-only QD dispersions typically display a pronounced blueshift in both absorption and emission upon dilution or after prolonged storage in a refrigerator.[11] This blueshift likely originates from surface-related changes induced by partial ligand loss, which modify the local dielectric environment and exciton confinement. Such alterations can affect the electronic structure and may ultimately reduce the effective core size in the presence of surface oxidation, resulting in a shift of both absorption and emission to higher energies. By contrast, in core–shell QDs the presence of a protective shell stabilizes the spectral positions of both absorption and emission (Fig. 2 and S11), indicating no dramatic changes in exciton confinement and therefore no significant shift in optical transitions. Furthermore, PL spectra of the samples remeasured after 8–10 months of refrigerated storage showed no changes in spectral positions or line shapes.

As mentioned earlier, InP/ZnS QDs exhibit type-I band alignment, implying that both electron and hole should be effectively confined within the InP core, especially given the thick ZnS shells used in this study. In principle, this should render the exciton insensitive to the shell surface. Our results, however, demonstrate that surface optoelectronic quality still plays a critical role in the PL of core–shell QDs. The evanescent tail of the confined electron or hole wavefunction penetrates the shell and can overlap with surface-defect orbitals. The electron is particularly prone to such capture owing to its lighter effective mass compared to the hole. The non-radiative carrier capture rate decreases approximately exponentially with both shell thickness and barrier height,[73] yet it never vanishes completely, even for very thick shells. For instance, effective suppression of Auger recombination in CdSe/CdS QDs requires so-called "giant" shells exceeding 12 CdS MLs.[74] Similarly, in InP/ZnSe/ZnS QDs the PL QY has been shown to increase continuously with ZnS shell growth up to 10 MLs.[52]

When the sample concentration is varied, the number of defect centres on the QD surface changes as a result of ligand desorption, as discussed above. Since the number of such quenchers scales with the QD surface area, we multiplied the relative molar concentrations (Fig. S9) by the corresponding surface areas $4\pi R^2$ (see Table 1) to estimate the relative total surface area of each ensemble. Fig. 7 replots the PL decay lifetimes and QY from Fig. 6 (or Fig. S9) using these converted units. After normalization, both observables collapse onto
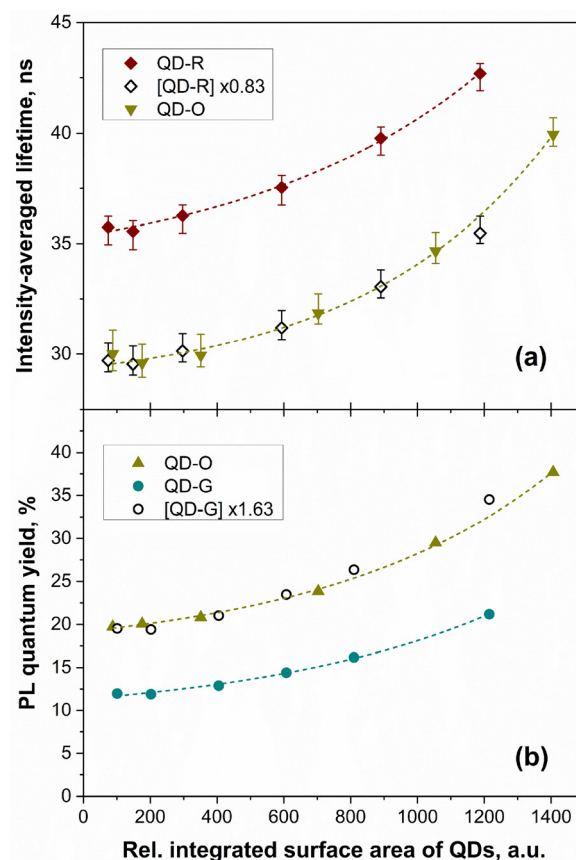

Fig. 7 Data from Fig. 6 plotted as a function of the relative integrated surface area of QDs, defined as ISA = $c_V \times 4\pi R^2$, where c_V is the relative molar concentration of dots and R the mean QD radius obtained from TEM. Panels show the intensity-averaged PL decay lifetime (a) and absolute QY (b), both recorded under 405 nm excitation, for QD-G (dark cyan circles), QD-O (dark yellow triangles) and QD-R (wine diamonds) ensembles. After normalization, both observables collapse onto nearly identical trends as a function of ISA, reinforcing the hypothesis that the observed quenching behaviour is governed by surface-related non-radiative processes.

nearly identical curves as a function of integrated surface area, supporting a surface-induced origin of the observed behaviour.

Furthermore, a direct correlation exists between PL QY (or lifetime) and both the shell thickness and the interfacial barrier height, parameters that are themselves linked to the core size (see Table 1). Comparing the QD-G, QD-O, and QD-R ensembles illustrates this relationship: from QD-G to QD-R, the shell becomes progressively thicker and the effective barrier height increases (owing to reduced QC), leading to systematically higher PL QY and longer decay lifetimes (Fig. 7).

This underscores the intrinsic challenge of fully isolating the exciton within the QD core from its surroundings, even in type-I heterostructures with thick shells. In the following section, we explore an approach to incorporating these colloidal heterostructures into polymer matrices.

3.5. Incorporation of QDs into PMMA and PDMS matrices

Colloidal dispersions of the QD-G ensemble were selected as a starting point. Aliquots of QDs in toluene were mixed with either PMMA or PDMS polymers, and solid (PMMA) or jelly-like (PDMS) samples were obtained after toluene evaporation (Fig. S15). Fig. 8 compares the PL QY of QD-G in these three environments. Incorporation into PMMA resulted in a modest ~25% additional loss, whereas embedding in PDMS caused severe quenching – nearly an order of magnitude reduction at low loading.

Several factors explain the markedly smaller PL QY loss in PMMA compared with PDMS. PMMA contains polar carbonyl (C=O) groups whose dipole moments enable favourable dipole–dipole and hydrogen-bond interactions with the native oleate ligands on the QD shell. These interactions reduce the desorption free energy, allowing the original passivation layer to remain intact during solvent removal and thereby limiting the formation of surface traps. In contrast, PDMS presents a

chemical mismatch between its non-polar –Si–O–Si– backbone and the oleate ligands, which promotes partial ligand stripping and even phase segregation of the QDs. Both effects enhance non-radiative surface recombination. Additionally, while PMMA samples are prepared simply by dissolving pre-polymerised PMMA in toluene, commercial PDMS kits often contain hydrosilane residues that are redox-active. These residues can diffuse to the QD interface and serve as efficient electron or hole traps. Finally, the steady-state dissolved O_2 concentration in liquid PDMS is significantly higher[75] than in PMMA, accelerating photo-oxidative trap formation during PL measurements.

4. Conclusions

In summary, this study elucidates the photophysical properties of OA-capped InP/ZnS core–shell QDs across green-, orange-, and red-emitting ensembles, revealing unexpected concentration dependence despite thick ZnS shells.

The optical characterization confirmed size-tuned absorption (507–618 nm) and emission (537–644 nm) peaks, with valley depths indicating varying polydispersity (narrowest for QD-G). Absorption analysis revealed first and second excitonic transitions (e.g., 2.43 eV and 2.79 eV for QD-G) via baseline subtraction and second-derivative methods, confirming band-edge origins aligned with PL. Excitation-wavelength-dependent PL QYs deviated from Vavilov's rule, exhibiting resonant enhancements, state-density dips, and sub-gap drops due to reabsorption and traps.

PL decay kinetics demonstrated non-exponential decays with spectral dispersion: lifetimes remained invariant (tens of ns) for smaller sub-ensembles but extended to hundreds of ns for larger ones, consistent with QC enhancing radiative rates.

Although the thick ZnS shells (6–13 monolayers) were expected to provide efficient electronic insulation via type-I band alignment, both PL QY and decay lifetimes exhibited strong concentration dependence. Specifically, both PL QYs and lifetimes decreased exponentially upon dilution in toluene (from 100% to 6.25% relative mass concentration), with radiative rates dropping 1.4-fold and non-radiative rates rising 1.7-fold. This universal trend, independent of reabsorption or energy transfer and observed across all ensembles, scaled with integrated surface area rather than particle number, arising from ligand desorption and surface trap formation on the one hand, and from wavefunction leakage from the core in spite of type-I confinement on the other.

Furthermore, polymer incorporation amplified these effects: PMMA induced modest QY losses via favorable dipole interactions preserving passivation, whereas PDMS caused drastic quenching from ligand stripping, possible phase segregation, and hydrosilane/oxygen traps. Our findings highlight the intrinsic incompatibility between native oleate ligands and pristine PDMS suggesting a requirement for ligand modification before PDMS film fabrication.[76] Overall, these results underscore that surface states dominate photophysics even in
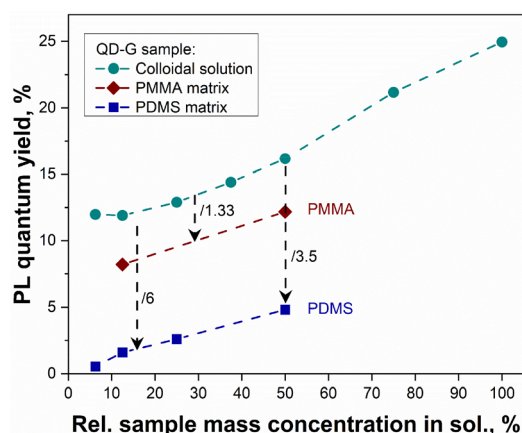

Fig. 8 Variations of PL QY of QD-G ensemble as a function of relative solids mass concentration in toluene solution. The original colloidal suspensions (dark cyan circles) were subsequently transferred into either PMMA (wine diamonds) or PDMS (dark blue squares) matrices. The dashed lines and arrows serve as eye-guides.

thick-shelled InP/ZnS QDs, limiting isolation of core excitons and emphasizing the need for improved passivation strategies to enhance stability in diluted or matrix-embedded applications.

This work enhances our understanding of quantum confinement and ligand-trap dynamics, refining models of radiative/non-radiative recombination. It offers valuable insights into stable, non-toxic QD development for optoelectronics (*e.g.*, displays) and biomedicine (*e.g.*, bioimaging), optimizing surface engineering for diluted or matrix-embedded stability.

Author contributions

Michael Greben: conceptualization, data curation, formal analysis, investigation, methodology, project administration, software, supervision, validation, visualization, writing – original draft, writing – review & editing. Dmytro Vorontsov: conceptualization, investigation, methodology, resources, writing – review & editing. Petro Khoroshyy: investigation, resources, validation, writing – review & editing. Michal Gulka: investigation, resources, validation, writing – review & editing. Jan Valenta: conceptualization, data curation, formal analysis, funding acquisition, investigation, methodology, project administration, supervision, validation, writing – review & editing.

Conflicts of interest

There are no conflicts to declare.

Data availability

Raw spectroscopic data (absorbance, PL quantum yield, and PL time transients) are available in the Zenodo repository (https://doi.org/10.5281/zenodo.17437002).

Supplementary information (SI): representative TEM micrographs. See DOI: https://doi.org/10.1039/d5nr03737a.

Acknowledgements

References

1 H. S. Chen, C. Y. Chen and Y. C. Wu, *Adv. Mater.*, 2025, **37**, 2407026.

2 J. Kim, J. Roh, M. Park and C. Lee, *Adv. Mater.*, 2024, **36**, 1–25.

3 B. Chen, D. Li and F. Wang, *Small*, 2020, **16**, 1–20.

4 J. Ye, D. Gaur, C. Mi, Z. Chen, I. L. Fernández, H. Zhao, Y. Dong, L. Polavarapu and R. L. Z. Hoye, *Chem. Soc. Rev.*, 2024, **53**, 8095–8122.

5 G. Almeida, R. F. Ubbink, M. Stam, I. du Fossé and A. J. Houtepen, *Nat. Rev. Mater.*, 2023, **8**, 742–758.

6 R. Toufanian, M. Chern, V. H. Kong and A. M. Dennis, *Chem. Mater.*, 2021, **33**, 1964–1975.

7 S. Shin, Y. Lee, J. Kim, J. Na, N. Gwak, S. Kim, J. Seo, C. S. Yoon and N. Oh, *Small Methods*, 2024, **2401560**, 1–9.

8 X. Zhou, Q. Hu and Y. Wang, *Chem. Eng. J.*, 2024, **488**, 151152.

9 P. Chen, H. Liu, Y. Cui, C. Liu, Y. Li, Y. Gao, J. Cheng and T. He, *J. Phys. Chem. C*, 2023, **127**, 2464–2470.

10 J.-H. Jo, D.-Y. Jo, S.-H. Lee, S.-Y. Yoon, H.-B. Lim, B.-J. Lee, Y. R. Do and H. Yang, *ACS Appl. Nano Mater.*, 2020, **3**, 1972–1980.

11 M. Greben, D. Vorontsov, R. Dědic, P. Khoroshyy, L. Ludvíková and J. Valenta, *Nanoscale*, 2025, **17**, 1602–1615.

12 M. Greben, P. Khoroshyy, I. Sychugov and J. Valenta, *Appl. Spectrosc. Rev.*, 2019, **54**, 758–801.

13 J. Valenta, A. Fucikova, M. Greben, H. S. Khan, R. Paolini, S. Garshasbi and M. Santamouris, *AIP Adv.*, 2024, **14**, 10–15.

14 J. Schindelin, I. Arganda-Carreras, E. Frise, V. Kaynig, M. Longair, T. Pietzsch, S. Preibisch, C. Rueden, S. Saalfeld, B. Schmid, J. Tinevez, D. J. White, V. Hartenstein, K. Eliceiri, P. Tomancak and A. Cardona, *Nat. Methods*, 2012, **9**, 676–682.

15 I. Pelant and J. Valenta, *Luminescence Spectroscopy of Semiconductors*, Oxford University Press, New York, 2012.

16 O. I. Micic, C. J. Curtis, K. M. Jones, J. R. Sprague and A. J. Nozik, *J. Phys. Chem.*, 1994, **98**, 4966–4969.

17 Z. Hens and J. C. Martins, *Chem. Mater.*, 2013, **25**, 1211–1221.

18 B. Fritzinger, I. Moreels, P. Lommens, R. Koole, Z. Hens and J. C. Martins, *J. Am. Chem. Soc.*, 2009, **131**, 3024–3032.

19 M. P. Weir, D. T. W. Toolan, R. C. Kilbride, N. J. W. Penfold, A. L. Washington, S. M. King, J. Xiao, Z. Zhang, V. Gray,

S. Dowland, J. Winkel, N. C. Greenham, R. H. Friend, A. Rao, A. J. Ryan and R. A. L. Jones, *J. Phys. Chem. Lett.*, 2019, **10**, 4713–4719.

20 J. De Roo, *Chem. Mater.*, 2023, **35**, 3781–3792.

21 A. Roberge, J. H. Dunlap, F. Ahmed and A. B. Greytak, *Chem. Mater.*, 2020, **32**, 6588–6594.

22 K. Nemoto, J. Watanabe, H.-T. Sun and N. Shirahata, *Nanoscale*, 2022, **14**, 9900–9909.

23 S. Haubold, M. Haase, A. Kornowski and H. Weller, *ChemPhysChem*, 2001, **2**, 331–334.

24 A. Narayanaswamy, L. F. Feiner and P. J. van der Zaag, *J. Phys. Chem. C*, 2008, **112**, 6775–6780.

25 M. Kuno, I. Gushchina, S. Toso and V. Trepalin, *J. Phys. Chem. C*, 2022, **126**, 11867–11874.

26 P. Ramasamy, N. Kim, Y.-S. Kang, O. Ramirez and J.-S. Lee, *Chem. Mater.*, 2017, **29**, 6893–6899.

27 J. R. Lakowicz, *Principles of Fluorescence Spectroscopy*, Springer US, Boston, MA, 2006.

28 D. Roy, S. Ghosh, C. K. De, S. Mukherjee, S. Mandal and P. K. Mandal, *J. Phys. Chem. Lett.*, 2022, **13**, 2404–2417.

29 B. Zhang, X. Wang, D. Wang, J. Tang, X. Fang, D. Fang, X. Wang, R. Chen, T. He and Z. Wei, *J. Phys. Chem. C*, 2019, **123**, 27207–27213.

30 Y. Xu, L. Yan, S. Fu and Y. Lv, *Chem. Phys. Impact*, 2024, **8**, 100579.

31 J. Hoy, P. J. Morrison, L. K. Steinberg, W. E. Buhro and R. A. Loomis, *J. Phys. Chem. Lett.*, 2013, **4**, 2053–2060.

32 M. D. Tessier, D. Dupont, K. De Nolf, J. De Roo and Z. Hens, *Chem. Mater.*, 2015, **27**, 4893–4898.

33 D. Debellis, G. Gigli, S. ten Brink, I. Infante and C. Giansante, *Nano Lett.*, 2017, **17**, 1248–1254.

34 R. K. Čapek, I. Moreels, K. Lambert, D. De Muynck, Q. Zhao, A. Van Tomme, F. Vanhaecke and Z. Hens, *J. Phys. Chem. C*, 2010, **114**, 6371–6376.

35 X. Ma, J. Min, Z. Zeng, C. S. Garoufalis, S. Baskoutas, Y. Jia and Z. Du, *Phys. Rev. B*, 2019, **100**, 245404.

36 A. F. Richter, M. Binder, B. J. Bohn, N. Grumbach, S. Neyshtadt, A. S. Urban and J. Feldmann, *ACS Nano*, 2019, **13**, 14408–14415.

37 P. Reiss, M. Protière and L. Li, *Small*, 2009, **5**, 154–168.

38 R. Toufanian, A. Piryatinski, A. H. Mahler, R. Iyer, J. A. Hollingsworth and A. M. Dennis, *Front. Chem.*, 2018, **6**, 1–12.

39 J. Zhao, R. Jiang, M. Huang, Y. Qiao, S. Wang, W. Zhang, P. Tian, J. Wang, R. Guo and S. Mei, *ACS Energy Lett.*, 2025, 2096–2132.

40 A. Narayanaswamy, L. F. Feiner, A. Meijerink and P. J. van der Zaag, *ACS Nano*, 2009, **3**, 2539–2546.

41 W. Yang, Y. Yang, A. L. Kaledin, S. He, T. Jin, J. R. McBride and T. Lian, *Chem. Sci.*, 2020, **11**, 5779–5789.

42 L. Li and P. Reiss, *J. Am. Chem. Soc.*, 2008, **130**, 11588–11589.

43 H. Liu, P. Chen, Y. Cui, Y. Gao, J. Cheng, T. He and R. Chen, *Adv. Opt. Mater.*, 2023, **11**, 1–23.

44 J. C. Lee, E.-P. Jang, D. S. Jang, Y. Choi, M. Choi and H. Yang, *J. Lumin.*, 2013, **134**, 798–805.

45 E. Cho, H. Jang, J. Lee and E. Jang, *Nanotechnology*, 2013, **24**, 215201.

46 P. Liu, Y. Lou, S. Ding, W. Zhang, Z. Wu, H. Yang, B. Xu, K. Wang and X. W. Sun, *Adv. Funct. Mater.*, 2021, **31**, 1–7.

47 Y. Bian, F. Chen, H. Shen and Z. Du, *J. Phys.: Condens. Matter*, 2022, **34**, 414005.

48 B. G. Kumar, S. Sadeghi, R. Melikov, M. M. Aria, H. B. Jalali, C. W. Ow-Yang and S. Nizamoglu, *Nanotechnology*, 2018, **29**, 345605.

49 X.-B. Fan, D.-W. Shin, S. Lee, J. Ye, S. Yu, D. J. Morgan, A. Arbab, J. Yang, J.-W. Jo, Y. Kim, S.-M. Jung, P. R. Davies, A. Rao, B. Hou and J. M. Kim, *Nanoscale Horiz.*, 2023, **8**, 522–529.

50 A. J. Zavaraki, Q. Liu and H. Ågren, *Nano-Struct. Nano-Objects*, 2020, **22**, 100461.

51 S. Rakshit, B. Cohen, M. Gutiérrez, A. O. El-Ballouli and A. Douhal, *ACS Appl. Mater. Interfaces*, 2023, **15**, 3099–3111.

52 F. Cao, S. Wang, F. Wang, Q. Wu, D. Zhao and X. Yang, *Chem. Mater.*, 2018, **30**, 8002–8007.

53 P. Reiss, M. Carrière, C. Lincheneau, L. Vaure and S. Tamang, *Chem. Rev.*, 2016, **116**, 10731–10819.

54 G. Almeida, L. van der Poll, W. H. Evers, E. Szoboszlai, S. J. W. Vonk, F. T. Rabouw and A. J. Houtepen, *Nano Lett.*, 2023, **23**, 8697–8703.

55 H. S. Shim, M. Ko, S. Nam, J. H. Oh, S. Jeong, Y. Yang, S. M. Park, Y. R. Do and J. K. Song, *ACS Appl. Nano Mater.*, 2023, **6**, 1285–1294.

56 J. Zhang, J. Wang, T. Yan, Y. Peng, D. Xu and D. Deng, *J. Mater. Chem. B*, 2017, **5**, 8152–8160.

57 K.-Z. Song, J.-Z. Huang, M.-X. Li and F.-L. Jiang, *ACS Appl. Mater. Interfaces*, 2025, **17**, 1542–1555.

58 I. Moreels, K. Lambert, D. Smeets, D. De Muynck, T. Nollet, J. C. Martins, F. Vanhaecke, A. Vantomme, C. Delerue, G. Allan and Z. Hens, *ACS Nano*, 2009, **3**, 3023–3030.

59 Y. Kayanuma, *Solid State Commun.*, 1986, **59**, 405–408.

60 L. E. Brus, *J. Chem. Phys.*, 1984, **80**, 4403–4409.

61 T. Takagahara, *Phys. Rev. B: Condens. Matter Mater. Phys.*, 1993, **47**, 4569–4584.

62 S. Adam, D. V. Talapin, H. Borchert, A. Lobo, C. McGinley, A. R. B. de Castro, M. Haase, H. Weller and T. Möller, *J. Chem. Phys.*, 2005, **123**, 1–10.

63 I. Angeloni, W. Raja, A. Polovitsyn, F. De Donato, R. P. Zaccaria and I. Moreels, *Nanoscale*, 2017, **9**, 4730–4738.

64 Y. Gao and X. Peng, *J. Am. Chem. Soc.*, 2015, **137**, 4230–4235.

65 A. F. van Driel, G. Allan, C. Delerue, P. Lodahl, W. L. Vos and D. Vanmaekelbergh, *Phys. Rev. Lett.*, 2005, **95**, 236804.

66 M. Lunz, A. L. Bradley, W.-Y. Chen, V. A. Gerard, S. J. Byrne, Y. K. Gun'ko, V. Lesnyak and N. Gaponik, *Phys. Rev. B: Condens. Matter Mater. Phys.*, 2010, **81**, 205316.

67 P. Roy, M. Virmani and P. P. Pillai, *Chem. Sci.*, 2023, **14**, 5167–5176.

68 G. Zatryb, A. Adamski, M. Chrzanowski, A. M. Żak and A. Podhorodecki, *Luminescence*, 2024, **39**, e4759.

69 M. Greben, A. Fucikova and J. Valenta, *J. Appl. Phys.*, 2015, **117**, 144306.

70 M. Grabolle, M. Spieles, V. Lesnyak, N. Gaponik, A. Eychmüller and U. Resch-Genger, *Anal. Chem.*, 2009, **81**, 6285–6294.

71 L. Hartmann, A. Kumar, M. Welker, A. Fiore, C. Julien-Rabant, M. Gromova, M. Bardet, P. Reiss, P. N. W. Baxter, F. Chandezon and R. B. Pansu, *ACS Nano*, 2012, **6**, 9033–9041.

72 G. Granados-Oliveros, B. S. G. Pineros and F. G. O. Calderon, *J. Mol. Struct.*, 2022, **1254**, 132293.

73 A. Jain, O. Voznyy, M. Korkusinski, P. Hawrylak and E. H. Sargent, *J. Phys. Chem. Lett.*, 2017, **8**, 3179–3184.

74 B. N. Pal, Y. Ghosh, S. Brovelli, R. Laocharoensuk, V. I. Klimov, J. A. Hollingsworth and H. Htoon, *Nano Lett.*, 2012, **12**, 331–336.

75 C. J. Ochs, J. Kasuya, A. Pavesi and R. D. Kamm, *Lab Chip*, 2014, **14**, 459–462.

76 B. Kim, Y. Choi, K. Lee and H. Chae, *J. Opt. Soc. Am. B*, 2024, **41**, 2488.